Determining transition state geometries in liquids using 2D-IR

James F. Cahoon, Karma R. Sawyer,* Jacob P. Schlegel,* and Charles B. Harris[†]

Many properties of chemical reactions are determined by the transition state connecting reactant and product, yet it is difficult to directly measure any information on these short-lived structures in liquids. We show that two dimensional infrared (2D-IR) spectroscopy provides direct information on transition states by tracking the transformation of vibrational modes as a molecule crosses a transition state. We successfully monitored a simple chemical reaction, the fluxional rearrangement of $Fe(CO)_5$; the exchange of axial and equatorial CO ligands causes an exchange of vibrational energy between the normal modes of the molecule. This energy transfer provides direct evidence for the time-scale, transition state, and mechanism of the reaction.

One-sentence summary: Ultrafast two-dimensional infrared spectroscopy is used to determine the time-scale and transition state of a simple chemical reaction, the exchange of carbonyls in $Fe(CO)_5$.

Transition states determine many properties of chemical reactions, yet there are limited experimental methods to directly probe the details of transition state geometries and symmetries in liquids. Molecular structures primarily reflect local minima on a potential energy surface and chemical reactions occur only during brief excursions up and over transition states on these surfaces. The excursions are short-lived, greatly complicating any measure of their properties. Most methods with sufficient time resolution rely on photoinitiation of a chemical reaction and provide information on the intermediates formed during the course of the reaction rather than direct information on transition state structures (*1*).

Here, we demonstrate that ultrafast two dimensional infrared (2D-IR) spectroscopy provides evidence for the transition state involved in a simple thermal chemical reaction, the fluxionality of $Fe(CO)_5$. Fluxionality refers to the rearrangement of a molecule between chemically indistinguishable structures. These reactions produce no net change in molecular structure, yet they are important for understanding the basic chemical behavior and reactivity of molecules in solution.

Department of Chemistry, University of California, Berkeley, California 94720, and Chemical Sciences Division, Lawrence Berkeley National Laboratory, Berkeley, California 94720
* These authors contributed equally and are listed alphabetically
† corresponding author email address: cbharris@berkeley.edu

Fe(CO)$_5$, an organometallic complex with five CO ligands arranged in a trigonal bipyramidal geometry, is a textbook example for fluxionality. In the late 1950s, nuclear magnetic resonance (NMR) spectroscopy revealed that this molecule rapidly exchanges its CO ligands between axial and equatorial sites. The ^{13}C NMR spectrum of ^{13}C labeled Fe(CO)$_5$ exhibits only a single peak at all accessibly measured solution temperatures, indicating that ^{13}C nuclei shift between axial and equatorial positions faster than NMR spectroscopy is able to distinguish these two chemical environments (2-4). Careful analysis of IR, Raman, and NMR spectra of Fe(CO)$_5$ and various derivatives suggests that the exchange process possesses a low barrier and occurs on a time-scale of picoseconds (4-6). Nevertheless, the dynamics in solution have not been quantified.

From a general perspective, fluxional processes are simple chemical reactions in which a molecule briefly rearranges to a new symmetry and geometry as it crosses a transition state and then returns to its original geometry as it completes the reaction. We show for Fe(CO)$_5$ that during this process energy is exchanged between the vibrational modes of the reactive ligands. Quantification of this energy exchange provides direct information on the time-scale, transition state, and consequently, mechanism of the reaction.

2D-IR spectroscopy has recently received much attention for its ability to monitor thermal reactions and chemical exchange on the femtosecond and picosecond time-scales. Conventionally, ultrafast timing of chemical reactions is achieved by photoinitiating the reactions with a short, intense laser pulse which electronically excites the molecules and typically leaves them with significant excess energy (1). In comparison, 2D-IR spectroscopy only requires vibrational excitation with an ultrafast IR laser pulse and allows the investigation of an entirely different class of thermally activated reactions in liquids at or close to equilibrium. Although similar to one-dimensional IR-pump, IR-probe experiments (1D-IR), 2D-IR spectroscopy separates the contributions to the 1D-IR spectrum into two frequency dimensions, which provides information on the correlations, anharmonicities, and exchange dynamics between all vibrational modes encompassed by the bandwidth of the laser pulses (7-9). This additional information is necessary to monitor thermal chemical reactions with ultrafast precision.

For example, Fayer and coworkers recently reported direct dynamics measurements of carbon-carbon single-bond rotation (10), and in similar experiments several groups have observed the complexation and

dissociation of solute-solvent complexes (*11-13*). These experiments use 2D-IR spectroscopy to vibrationally tag a specific, localized vibrational mode and monitor its shift in frequency as the system undergoes chemical dynamics. Here we demonstrate a conceptually different experiment on $Fe(CO)_5$. We are imparting vibrational energy into a specific but delocalized vibrational mode and monitoring how that energy is distributed between the delocalized modes as the molecule crosses a transition state. Quantification of this energy exchange provides direct information on the time-scale, transition state, and consequently, mechanism of the reaction.

$Fe(CO)_5$ has two IR active vibrational modes involving the stretch of the CO ligands. For the D_{3h} symmetry of $Fe(CO)_5$, these absorptions correspond to a doubly degenerate e' band and an a_2'' band, respectively at 1999 and 2022 cm^{-1} in *n*-dodecane solution (Fig. 1A). Density functional theory (DFT) vibrational frequency calculations (*14*) yield CO displacements for the a_2'' and e' modes as illustrated in Fig. 1B. The e' mode involves nearly exclusive vibration of the three equatorial CO groups whereas the a_2'' mode involves vibration of the axial CO groups.

In principal, fluxionality can cause the coalescence and collapse of the two IR absorptions into a single peak, analogous to the coalescence of line shapes observed in NMR spectra. The frequency of exchange must be comparable to the frequency separation of the absorption bands, which is ca. 1 ps^{-1} for these absorptions. The Fourier transform (FT) IR spectrum at 100 ˚C shows some evidence of coalescence relative to the room temperature spectrum (Fig. 1A), but it is unclear if the changes in line shape are the result of exchange or homogenous broadening (see Fig. S1). The boiling point (103 ˚C) and thermal instability of $Fe(CO)_5$ prevent acquisition of spectra at sufficiently high temperatures to conclusively observe IR coalescence. Nevertheless, several examples of this phenomenon have been reported and attributed to fast exchange (*15-17*), yet the true physical origin of the effect has been debated in some instances (*18*). The 2D-IR spectra reported below, however, show strong evidence for the time-scale of fluxionality and exchange in room-temperature solution and highlight the advantage of 2D-IR as a more general method of observing IR exchange, analogous to the advantages of 2D-NMR over conventional NMR spectroscopy (*19*).

The experiment proceeds as follows. First, a narrowband IR laser pulse selectively excites one of the two vibrational bands in $Fe(CO)_5$, promoting it from the $v = 0$ to $v = 1$ vibrational level. Second, a fixed time elapses (referred to as the waiting time, T_w) to allow the molecule to exchange axial and equatorial ligands. Third, a broadband IR laser pulse probes the sample, and the resulting absorption spectrum reflects how the vibrational energy imparted by the first pulse has been redistributed between the vibrational modes. The relative polarization between the two laser pulses is set to the magic angle (54.7˚) to avoid effects from rotational diffusion. This setup (20), based on a pump-probe style experiment (21), gives a time resolution of ca. 1 ps and eliminates many of the coherence transfer effects which are observed in heterodyne-detected photon echo 2D-IR experiments (8).

2D-IR spectra of $Fe(CO)_5$, normalized to the strongest peak at each T_w, are displayed in Fig. 2 for T_w of 2 ps, 7.5 ps, and 20 ps, and spectra acquired at additional T_w are provided in Fig. S3. The vertical axis represents the frequency of the narrowband IR pulse used to selectively excite vibrational modes, and the horizontal axis represents the change in absorbance resulting from this excitation after the waiting time T_w. Interpretation of this type of spectrum has been discussed extensively (7). Negative signals are shown in blue and appear along the diagonal at (2022, 2022) and (1999, 1999), which correspond to the 0-1 transition frequencies for the a_2'' and e' modes, respectively. Shifted down in frequency along the horizontal axis from the diagonal are positive peaks shown in red, corresponding to the 1-2 transition frequencies. These peaks are shifted off the diagonal by the anharmonicity of the vibrational potential. Note that the 0-1 peaks result both from bleaching of the ground state and stimulated emission from the excited state whereas the 1-2 peaks result from only $v = 1$ to $v = 2$ transitions (22). Unlike 2D-IR experiments on solute-solvent complexes (12, 13), all vibrational modes in these spectra share one common ground state level, and as a result, the exchange dynamics apparent in both the 0-1 and 1-2 signals only reflect dynamics in the excited vibrational states. The following analysis uses kinetic data from the 0-1 signal because these absorption line shapes are narrower and clearly defined on the diagonal and off-diagonal.

A significant shift in the peak intensities is observed between $T_w = 2$ and 7.5 ps (Fig. 2B). The most noticeable change is the increase in intensity at the cross peak positions, labeled as triangles in panels A to C. Several factors affect the relative intensities of peaks in 2D spectra, and cross peaks typically arise from

anharmonic coupling between vibrational modes. In order to predict the intensity of anharmonic cross peaks between the a_2'' and e' modes, DFT anharmonic frequency calculations (*14, 23*) were performed, giving an anharmonicity of 0.6 cm^{-1} between the two modes. Because the anharmonic shift is much smaller than the vibrational line widths, the contribution of these peaks to the 2D spectra is present but relatively minor. Vibrational relaxation may also contribute to changes in the peak intensities (*24*); however, vibrational relaxation of the CO stretches occurs on a much longer time scale (ca. 150 ps, Fig. S2) than the values of T_w in Fig. 2. and does not affect the interpretation of the spectra, as discussed further in the SOM.

The change in intensity at the diagonal and cross peak positions is attributed to vibrational energy transfer between the CO normal modes as $Fe(CO)_5$ crosses the transition state. Panels D to F of Fig. 2 show simulated 2D-IR spectra using DFT calculated anharmonic parameters (including the cross anharmonicity of 0.6 cm^{-1}) and assuming energy exchange (as described below) between the vibrational modes. The simulated spectra qualitatively reproduce the experimental data, indicating that the changes in peak intensity do result from vibrational energy transfer.

The most straightforward manner to see the energy exchange in the experimental data is to plot the ratio of off-diagonal (triangles) to diagonal (circles) peak intensities for the two horizontal slices of the 2D-IR spectra at ω_{pump} = 1999 and 2022 cm^{-1}. Data were collected for a range of waiting times T_w between 2 and 40 ps, and Fig. 3A displays these ratios as a function of T_w. For excitation of the a_2'' band, the ratio rises to an asymptotic value of 2, and for excitation of the e' band to an asymptotic value of 0.5.

In order to quantitatively understand the vibrational energy transfer and asymptotic values shown in Fig. 3A, the details of the molecular rearrangement must be considered. R. Stephen Berry proposed a pseudo-rotation mechanism for this type of trigonal bipyramidal complex: the D_{3h} equilibrium structure rearranges to a transition state with C_{4v} symmetry and then returns to the D_{3h} structure (*5, 25*). In the process, the two axial ligands are exchanged with two equatorial ligands at the transition state and the molecule appears to have rotated by 90˚. We have modeled this mechanism with DFT calculations of the intrinsic reaction coordinate (*14, 26*), with the results shown in Fig. 4A. The calculations give an electronic energy barrier of 2.13 kcal/mol.

In order to model the vibrational energy transfer observed in the 2D-IR spectra, we first assume the delocalized normal modes of $Fe(CO)_5$ can be expressed as linear combinations of the individual, localized CO stretch displacements (eq. 1):

$$|n\rangle = \sum_{j=1}^{5} |CO_j\rangle\langle CO_j|n\rangle, \tag{1}$$

where $|n\rangle$, $n = 1\ldots5$, represents the five harmonic normal modes composed of CO stretches and $|CO_j\rangle$ $j = 1\ldots5$ represents the displacement vector of the jth CO group. Neglecting changes in this displacement vector as the CO groups change position (i.e. neglecting changes in the local mode force constants and wavefunctions), the initial normal mode $|n_i\rangle$ before rearrangement of the molecule can be expressed as a superposition of the normal modes $|n_f\rangle$ after rearrangement as in eq. 2,

$$|n_i\rangle = \sum_{n=1}^{5} |n_f\rangle \sum_{j=1}^{5} \langle n_f|CO_j\rangle\langle CO_j|n_i\rangle, \tag{2}$$

where the individual CO groups $|CO_j\rangle$ retain their label j as they rearrange. This analysis was performed assuming the pseudo-rotation mechanism by projecting the initial CO normal modes, including the two IR inactive a_1' modes, onto the C_{4v} transition state and then onto the rearranged D_{3h} structure using the DFT calculated vibrations. The results are summarized schematically in Fig. 4B, where the states $|n\rangle$ are labeled by their corresponding symmetries, and coefficients, as calculated from eq. 2, are provided in front of these labels. Note that the irreducible representations and projections for the vibrations would be different for transition states with different symmetries.

In order to model vibrational energy transfer, we need the probability that the initial vibration $|n_i\rangle$ will transfer energy into a final normal mode $|n_f\rangle$, which is given by eq. 3,

$$P_{n_i \to n_f} = \left| \sum_{j=1}^{5} \langle n_f|CO_j\rangle\langle CO_j|n_i\rangle \right|^2, \tag{3}$$

and these values are given in the far right column of Fig. 4B as percentages. Based on these values, we have simulated energy transfer in $Fe(CO)_5$ using a simple deterministic rate law governed by one rate

constant k, the rate of crossing the barrier in the fluxional reaction. The rate of transferring energy from one initial mode into a final vibrational mode is given by eq. 4,

$$k_{n_i \to n_f} = P_{n_i \to n_f} \times k ,$$ (4)

and the kinetics for energy transfer among all the normal modes have been calculated using standard finite difference methods (*27*).

Based on this analysis, 2D-IR data were simulated with energy transfer included as shown in Fig. 2 panels D to F. In addition, the ratios of off-diagonal to diagonal peak intensity, which directly reflect the relative populations of the e' and a_2'' vibrational modes, were simulated using this model. The best agreement with the experimental data at room temperature (18 ˚C) was achieved with a time constant of 8.0 $\pm$ 0.6 ps, or equivalently $k = 1/8$ ps^{-1}, and details of the procedure used to simulate and fit the data are provided in the SOM. The results of the simulation are shown as solid lines through the data in Fig. 3A. The good agreement of the simulations with the experimental data suggests that this model is sufficient to describe the vibrational energy exchange.

Both the simulations and experimental data show that the initial vibrational excitation rapidly reaches an equilibrium between the two IR active vibrational modes. Because there are two degenerate e' modes and only one a_2'' mode, this equilibration causes the off-diagonal to diagonal ratios in Fig. 3A to asymptotically approach the values 2 e' : 1 a_2''. If the molecules crossed the transition state only once, we would expect the asymptotic values would instead reflect the percentages in Fig. 4B. This case would be expected for reactions in which the product is thermodynamically stable compared to the reactant. In this experiment, however, the reactant and product are energetically equivalent and the barrier to the transition state is low, allowing the molecules to cross the transition state multiple times.

We have estimated the distribution of transition state crossings as a function of the waiting time T_w using Gillespie's Monte-Carlo algorithm to model the reaction as a stochastic process within the Markov approximation (*27, 28*). The distribution is displayed in Fig. 3B and shows that within 8 ps, approximately 25% of the molecules have crossed the transition state two or more times. Multiple crossings allow the fast exchange of energy between the vibrational modes and cause complete equilibration of the energy within a

few crosses of the transition state. The rate of equilibration depends both on the rate of the fluxional reaction and the details of the energy redistribution, which are determined by the transition state symmetry and, hence, mechanism of the rearrangement.

Although the pseudo-rotation has been widely accepted as the most likely mechanism for fluxionality in trigonal bipyramidal complexes like $Fe(CO)_5$, other possibilities have not been ruled out (*29*). The analysis of 2D-IR data described above requires the assumption of a mechanism and a transition state geometry in order to simulate the energy transfer process. To explore alternative pathways, we simulated data for a different fluxional mechanism in which one axial CO and two equatorial CO groups execute a twist motion, resulting in the exchange of one axial and one equatorial ligand. This mechanism predicts different energy exchange dynamics than the pseudo-rotation mechanism, the details of which are provided in the SOM. We found that reasonable agreement with the experimental data at room temperature (18 ˚C) could be achieved only with a much shorter time constant of 3.5 ± 0.4 ps for the twist rearrangement. The difference in time constant between the twist and pseudo-rotation mechanisms demonstrates that the experiment is sensitive to the mechanism, but because of fast multiple crossings, the data at room-temperature alone do not definitively support just one mechanism. Experiments at different temperatures, however, provide the additional data necessary to rule out the twist mechanism.

2D-IR data were collected at two additional temperatures and a kinetic analysis based on a pseudo-rotation was performed at all three temperatures, giving time constants of 8.0 ± 0.6 ps at room temperature (18 ˚C), 6.3 ± 0.8 ps at 50 ˚C, and 4.6 ± 0.4 ps at 90 ˚C. An Arrhenius plot of the data (Fig. S5) gives a straight line with an activation energy of 1.6 ± 0.3 kcal/mol. This result is in reasonable agreement with the barrier for the pseudo-rotation mechanism calculated by DFT (2.13 kcal/mol). In contrast, our DFT calculations on the twist mechanism, detailed in the SOM, indicate that the barrier for this type of rearrangement is at least one order of magnitude greater than the pseudo-rotation mechanism.

The Arrhenius plot not only further confirms the pseudo-rotation mechanism, but also demonstrates that the energy transfer results from a barrier crossing process and not intramolecular vibrational relaxation (IVR) caused by anharmonic coupling between the modes. IVR typically occurs on a time scale of picoseconds and could potentially compete with fluxionality as the cause of energy exchange between the

e' and a_2'' modes. The rate of IVR depends on the strength of the coupling as well as the existence of liquid phonons (instantaneous normal modes of the solvent) at the frequency of the energy mismatch between the modes (22.8 cm^{-1}), which serve to receive or supply the energy difference (*30, 31*). At higher temperatures, an increase in the population of low frequency phonons around 22.8 cm^{-1} may increase the rate of IVR. Because this frequency is low compared to the thermal energy in these experiments (200-260 cm^{-1}), the population will increase relatively little with temperature. Between 18 and 90 ˚C, we would expect the IVR rate to increase by ~26% (see SOM for description of this estimate), yet we observe a change in rate three times greater over this temperature range. IVR is also not supported by the DFT calculations, which predict a weak coupling between these modes (0.6 cm^{-1}) in comparison to other documented examples of IVR (*8, 32*). The 2D-IR data thus strongly support a fluxionality mechanism in which $Fe(CO)_5$ exchanges CO groups and vibrational energy through the C_{4v} transition state of the pseudo-rotation mechanism on a time-scale of 8 ps.

In extending the present technique to other systems, the interpretation of the data should be especially straightforward in cases where the system crosses the transition state only once. Even in more complex cases, we anticipate broad applications toward solution phase transition state characterization of both thermal and photoinitiated reactions.

References and Notes

1.   E. T. J. Nibbering, H. Fidder, E. Pines, *Annu. Rev. Phys. Chem.* **56**, 337 (2005).

2.   F. A. Cotton, A. Danti, J. S. Waugh, R. W. Fessenden, *J. Chem. Phys.* **29**, 1427 (1958).

3.   R. Bramley, R. S. Nyholm, B. N. Figgis, *Trans. Faraday Soc.* **58**, 1893 (1962).

4.   H. W. Spiess, R. Grosescu, U. Haeberle, *Chem. Phys.* **6**, 226 (1974).

5.   R. K. Sheline, H. Mahnke, *Angew. Chem., Int. Ed. Engl.* **14**, 314 (1975).

6.   J. K. Burdett, J. M. Grzybowski, M. Poliakoff, J. J. Turner, *J. Am. Chem. Soc.* **98**, 5728 (1976).

7.   M. Khalil, N. Demirdoven, A. Tokmakoff, *J. Phys. Chem. A* **107**, 5258 (2003).

8.   M. Khalil, N. Demirdoven, A. Tokmakoff, *J. Chem. Phys.* **121**, 362 (2004).

9.   Y. S. Kim, R. M. Hochstrasser, *J. Phys. Chem. B* **111**, 9697 (2007).

10.   J. R. Zheng, K. W. Kwak, J. Xie, M. D. Fayer, *Science* **313**, 1951 (2006).

11. S. Woutersen, Y. Mu, G. Stock, P. Hamm, *Chem. Phys.* **266**, 137 (2001).

12. J. R. Zheng, K. Kwak, J. Asbury, X. Chen, I. R. Piletic, M. D. Fayer, *Science* **309**, 1338 (2005).

13. Y. S. Kim, R. M. Hochstrasser, *Proc. Natl. Acad. Sci. U.S.A.* **102**, 11185 (2005).

14. DFT calculations were performed at the BP86 level using the basis sets 6-31+g(d) for C and O and LANL2DZ for Fe with the program Gaussian 03, Revision C.02, M. J. Frisch, *et. al.*, Gaussian, Inc., Wallingford CT, 2004.

15. C. H. Londergan, C. P. Kubiak, *Chem. Eur. J.* **9**, 5962 (2003).

16. F. W. Grevels, K. Kerpen, W. E. Klotzbucher, R. E. D. McClung, G. Russell, M. Viotte, K. Schaffner, *J. Am. Chem. Soc.* **120**, 10423 (1998).

17. Y. S. Kim, R. M. Hochstrasser, *J. Phys. Chem. B* **110**, 8531 (2006).

18. H. L. Strauss, *J. Am. Chem. Soc.* **114**, 905 (1992).

19. J. B. Lambert, E. P. Mazzola, *Nuclear Magnetic Resonance Spectroscopy*. (Pearson Education, Inc., Upper Saddle River, 2004).

20. Materials and methods are detailed in the Supporting Online Material available at Science Online.

21. J. Bredenbeck, J. Helbing, P. Hamm, *J. Chem. Phys.* **121**, 5943 (2004).

22. S. Mukamel, *Principles of Nonlinear Optical Spectroscopy*. (Oxford University Press, Inc., New York, 1995).

23. V. Barone, *J. Chem. Phys.* **122**, 014108 (2005).

24. D. V. Kurochkin, S. R. G. Naraharisetty, I. V. Rubtsov, *Proc. Natl. Acad. Sci. U.S.A.* **104**, 14209 (2007).

25. R. S. Berry, *J. Chem. Phys.* **32**, 933 (1960).

26. C. Gonzalez, H. B. Schlegel, *J. Chem. Phys.* **90**, 2154 (1989).

27. J. I. Steinfeld, J. S. Francisco, W. L. Hase, *Chemical Kinetics and Dynamics*. (Prentice-Hall, Inc., Upper Saddle River, ed. 2, 1989).

28. D. T. Gillespie, *J. Phys. Chem.* **81**, 2340 (1977).

29. I. Ugi, D. Marquard, H. Klusacek, P. Gillespie, F. Ramirez, *Acc. Chem. Res.* **4**, 288 (1971).

30. H. J. Bakker, *J. Chem. Phys.* **98**, 8496 (1993).

31. A. Tokmakoff, B. Sauter, M. D. Fayer, *J. Chem. Phys.* **100**, 9035 (1994).

32. J. D. Beckerle, M. P. Casassa, R. R. Cavanagh, E. J. Heilweil, J. C. Stephenson, *Chem. Phys.* **160**, 487 (1992).

33. We thank Peter Hamm and Jan Helbing for recommendations on the experimental apparatus. This work was supported by the NSF's Division of Physical Chemistry. We also acknowledge some specialized equipment supported by the DOE Office of Basic Energy Sciences, Chemical Sciences Division, under contract DE-AC02-05CH11231 and contractor supported research (CSR). J.F.C acknowledges an NSF graduate research fellowship.

Fig 1. (**A**) Room-temperature (25 °C) FTIR spectrum (solid line) of $Fe(CO)_5$ in *n*-dodecane and spectrum at 100 °C (dashed line) (**B**) Depiction of the approximate eigenvectors for the a_2'' and doubly degenerate e' vibrational modes of $Fe(CO)_5$.

Fig. 2. Contour plots of experimental 2D-IR spectra (top row) for $Fe(CO)_5$ in *n*-dodecane at room temperature (18 °C) acquired at waiting times of T_w = 2 ps (**A**), 7.5 ps (**B**), and 20 ps (**C**). Simulated 2D-IR data for the same waiting times are shown in the bottom row; panels **D**, **E**, and **F**, respectively. The data are normalized to the maximum absorption at each T_w, which corresponds to the negative absorption (blue) of the e' vibrational mode (see Fig. S2 for the absolute magnitude of this absorption), and contour lines represent a 10% change in absorption intensity. Diagonal peaks are marked by circles and off-diagonal peaks by triangles in panels **A** to **C**. Arrows in panel **B** represent vibrational energy exchange. Simulations (panels **D** to **F**) include energy exchange from a pseudo-rotation with a time constant of 8 ps, and details of the simulation parameters are provided in the SOM.

Fig. 3. (**A**) Ratio of 2D-IR off-diagonal to diagonal peak intensity at room temperature (18 °C) as a function of the waiting time T_w for selective excitation of the e' band (squares) and a_2'' band (diamonds). Ratios are calculated from Lorentzian fits to one-dimensional horizontal slices of the 2D-IR spectra using the intensities for peaks marked by circles and diamonds in Fig. 2. Solid lines are simulations assuming energy exchange due to the pseudo-rotation; a single time constant of 8 ± 0.6 ps gives the best fit for both curves. (**B**) The distribution of the number of transition state crossings as a function of the waiting time T_w for a fluxional process with a kinetic time constant of 8 ps

Fig. 4. (**A**) Depiction of the mechanism and energetics of a pseudo-rotation plotted as a function of the bond angle (C–Fe–C) between one axial and one equatorial CO ligand which exchange during the pseudo-rotation. Circles are DFT calculated energies along the intrinsic reaction coordinate, which gives a barrier height of 2.13 kcal/mol. Symmetry labels for the molecule as it passes over the barrier are provided above the structures. (**B**) The splitting of the vibrational modes, denoted by their symmetry labels, as the molecule crosses the transition state. The irreducible representation, Γ_{CO}, for vibrations of the CO groups is given at the top of each column. The individual vibrational modes in the starting structure becomes a superposition of

vibrational modes in the transition state and then again in the final rearranged structure, with the coefficients given for each mode in the superposition. The mixing is limited to those modes which are allowed to mix by symmetry. The final distribution of energy after one cross over the transition state is shown on the far right in percentages.

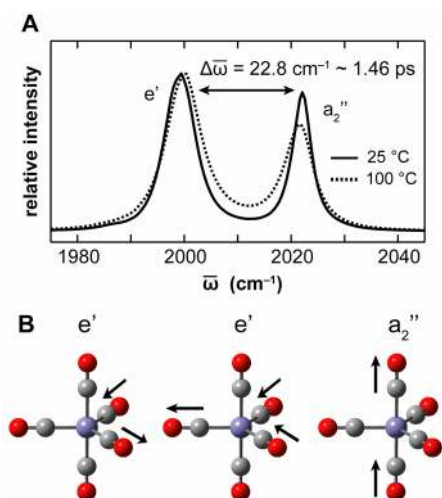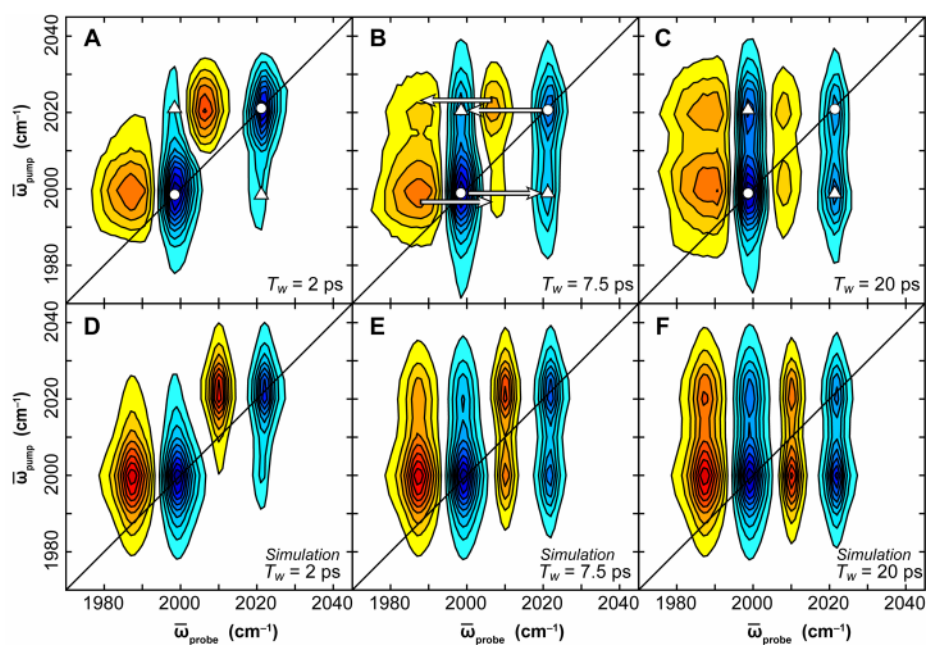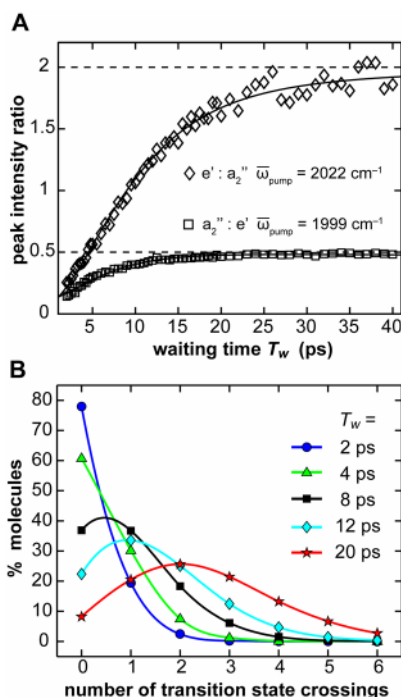Note that all figures have been submitted to *Science* as individual .eps files and the images below are for reviewing purposes only.

Fig. 1

Fig. 2
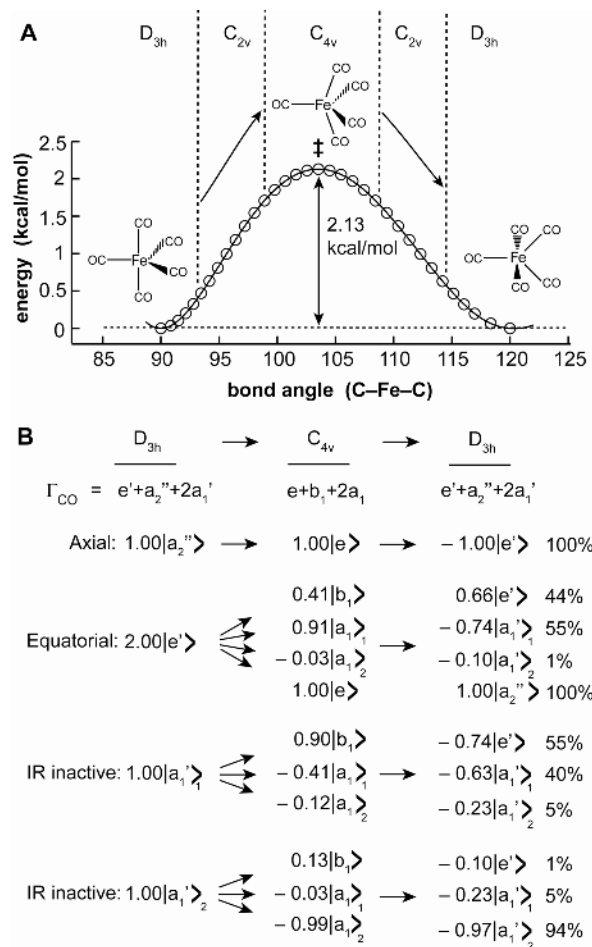
Fig. 3

Fig. 4

Determining transition state geometries in liquids using 2D-IR

James F. Cahoon, Karma R. Sawyer,* Jacob P. Schlegel,* and Charles B. Harris[†]

Contents

Figures

Department of Chemistry, University of California, Berkeley, California 94720, and Chemical Sciences Division, Lawrence Berkeley National Laboratory, Berkeley, California 94720
* These authors contributed equally and are listed alphabetically
[†] corresponding author email address: cbharris@berkeley.edu

I.   Materials and Methods

A.   Materials

Chemical samples were purchased from Sigma-Aldrich Co. and used without further purification. Solutions of Fe(CO)$_5$ in anhydrous *n*-dodecane were prepared under nitrogen atmosphere in a glove-box (Vacuum Atmospheres Company) and diluted to achieve a concentration of approximately 1.5 mM and a peak optical density of ca. 0.5.

B.   Two dimensional infrared (2D-IR) spectroscopy

The experimental apparatus consists of a Ti:sapphire regenerative amplifier (SpectraPhysics, Spitfire) seeded by a Ti:sapphire oscillator (SpectraPhysics, Tsunami) to produce a 1-kHz pulse train of 100-fs pulses centered at 800 nm with an average pulse energy of 0.9 mJ. Approximately 0.6 mJ is used to pump a homebuilt two-pass BBO-based optical parametric amplifier (OPA), the output of which is mixed in a AgGaS crystal to produce mid-infrared pulses at the difference frequency tunable from 3.0 to 6.0 μm with a spectral width of ca. 150 cm^{-1} and pulse duration around 100 fs (*S1*). This mid-infrared pulse is then split into three beams using a wedged ZnSe substrate. The reflections off the front and back surfaces are used as probe and reference beams, respectively. The transmitted beam is used as the infrared pump beam and is passed through a computer-controlled Fabry-Perot interferometer based on the design used by Peter Hamm and co-workers (*S2, S3*). The Fabry-Perot narrows the spectrum of the infrared pulse from an approximately 150 cm^{-1} full-width at half maximum (FWHM) to approximately 11 cm^{-1} FWHM and extends the temporal duration of the pulse to approximately 1 ps. The exact spectral width of this narrowband infrared pulse is recorded during the experiment and used in the simulation of the experimental data.

After the Fabry-Perot, the beam passes through an achromatic (λ = 4.5–6 μm) CdS/CdSe half-wave plate (Cleveland Crystals, Inc.) held in a computer-controlled rotation stage (Newport Corp., RGV100). Using this rotation stage, the polarization of the pump beam with respect to the probe beam is set to the magic angle, 54.7˚, to eliminate effects from rotational diffusion and ensure the experiment measures only population dynamics. The pump beam is passed through a computer controlled delay stage (Newport Corp., XMS-160) and then overlapped with the probe beam and focused onto the sample using a

10-cm focal-length off-axis unprotected gold-coated parabolic mirror (Janos Tech.), producing spot sizes of approximately 200 μm. Using a 150-μm thick, polished germanium wafer (Surface Process Group, LLC.), the pump and probe beams are cross-correlated at the sample and time zero is identified as the rising edge of the infrared pump pulse. The sample is held in a cell (Harrick Scientific) that is fitted with 2-mm thick non-birefringent CaF_2 windows (Crystran Ltd.) and that has a path length of 250 μm. For experiments above room temperature, a similar cell (Harrick Scientific) fitted with cartridge heaters and a thermocouple was used, which maintained the desired temperature within 0.5 ˚C as measured by the thermocouple embedded in the stainless steel construction around the windows and sample volume.

Directly after the sample, the probe beam is passed through a ZnSe wire-grid polarizer (Thorlabs, Inc.) set for maximum transmission at the probe beam polarization, and the probe beam is then recollimated with a second off-axis parabolic mirror. During data collection, the probe and reference beams are sent along a parallel path through a computer controlled spectrograph (Acton Research Corporation, SpectraPro-150) with entrance slits routinely set at 50 μm to achieve a spectral resolution of ca. 3 cm^{-1}. Spectrally dispersed probe and reference beams are detected by a 2x32 element MCT-array infrared detector (Infrared Associates, Inc.) using a high speed signal acquisition system and data acquisition software (Infrared Systems Development Corp.). Differences in optical density (ΔOD) as small as $\Delta OD = 10^{-5}$ can easily be observed within two seconds of data collection. In order to change the center frequency of the Fabry-Perot filter, the pump beam is directed into the spectrograph as required. Drifts in the center frequency of the pump beam during data collection are less than 1 cm^{-1}.

Broadband IR pump, IR probe measurements were made using the same experimental setup described above by removing the Fabry-Perot cavity from the IR pump beam path. Cross correlation of the IR pump and probe beams gives an instrument response of ca. 200 fs for this experiment.

C.   Fourier transform infrared (FTIR) spectroscopy

FTIR spectra were collected with a Thermo Nicolet Avatar 370 FTIR spectrometer with a spectral resolution of 1 cm^{-1}. Temperature dependent data were collected using the same temperature-controlled sample cell described in section IB. In order to prevent sample degredation due to the thermal instability of $Fe(CO)_5$, spectra were collected within two minutes of the sample cell reaching the desired temperature.

D.   Data analysis

Fits to the FTIR and 2D-IR experimental data were performed using the Nelder-Mead simplex algorithm to iteratively find the best fit parameters by the method of least squares (*S4*). For fits of the 2D-IR data (e.g. Fig. 3A), errors were calculated with a bootstrap fitting method in which the experimental data was simulated 500 times using a Monte Carlo method to sample each data point within a Gaussian distribution determined by the standard deviation calculated from five or more repeated measurements. Each simulation was then fit as decribed in section IVB using the simplex algorithm. The resulting distribution of best fit parameters was fit to a Gaussian distribution, and cited errors are two standard deviations corresponding to this Gaussian distribution. The errors represent uncertainty resulting from noise in the experimental data and are not meant as an estimate of any systematic error in the analysis.

The IR pump-probe data (Fig. S2A) was fit to single exponential function convoluted with a Gaussian function (full-width at half maximum (FWHM) of 200 fs) to accurately reflect the instrument response function. The Levenberg-Marquet least squares algorithm was used to find the best fit parameters, and the cited error corresponds to one standard deviation.

II.   Temperature-dependent FTIR spectra

The coalescence of absorption lines in nuclear magnetic resonance (NMR) spectroscopy has been observed for many compounds, yet the coalescence of absorptions in linear IR spectra has been observed in only a handful of instances. Most recently, Hochstrasser and coworkers reported IR spectra of acetonitrile dilute in methanol, a system which undergoes hydrogen bond exchange on the picosecond time-scale (*S5*). At low temperatures (-17 ˚C), the CN stretch on acetonitrile gives rise to two peaks corresponding to hydrogen-bonded and non-hydrogen bonded molecules. At high temperatures (80 ˚C), however, these two peaks coalescence in both the linear and 2D-IR spectra due to fast hydrogen bond exchange. In a very different system, Kubiak and coworkers observed the coalescence of FTIR absorptions on trinuclear ruthenium clusters which undergo rapid intramolecular electron transfer between the metal centers (*S6, S7*). The electron transfer causes a coalescence of the absorptions for the CO groups on the metal centers, and this effect was used to extract the rates of intramolecular electron transfer in these systems. The rapid

fluctuation of hydrogen bonds or transfer of electrons are both distinctly different physical processes than fluxionality, yet all three can significantly affect the IR spectra under the proper conditions.

The only example of IR coalescence resulting from fluxionality (of which we are aware) is for the complex $Fe(CO)_3(\eta^4$-1,5-cyclooctadiene), the linear IR spectrum of which has been reported several times (*S8-13*). Grevels, McClung, and coworkers modeled the changes in lineshape with temperature in terms of exchange and were able to extract rate constants for the exchange process by systematically fitting the spectra at multiple temperatures. Nevertheless, it has been debated whether the changes in lineshape can be equally well explained by other physical processes (*S14*). Here we report an analysis on the linear IR spectra of $Fe(CO)_5$ which highlights the limitations of linear IR spectroscopy and the advantage of 2D-IR spectroscopy as a more general method of observing IR exchange.

FTIR spectra in the CO stretching region of $Fe(CO)_5$ were measured at several temperatures between 25 and 150 ˚C and are shown in Fig. S1A normalized to the intensity of the e' vibrational mode of $Fe(CO)_5$. Above 100 ˚C, the sample was not stable due both to the boiling point (103 ˚C) and thermal instability of $Fe(CO)_5$. Nevertheless, the sample temperature was ramped at a sufficient rate (ca. 10 ˚C per minute) to collect FTIR spectra at 125 and 150 ˚C before decomposition of the sample. We were unable to collect a spectrum at 175 ˚C. The FTIR spectra show progressive changes as the temperature is raised, with the most notable change the increase in absorption intensity between the two vibrational bands. This effect
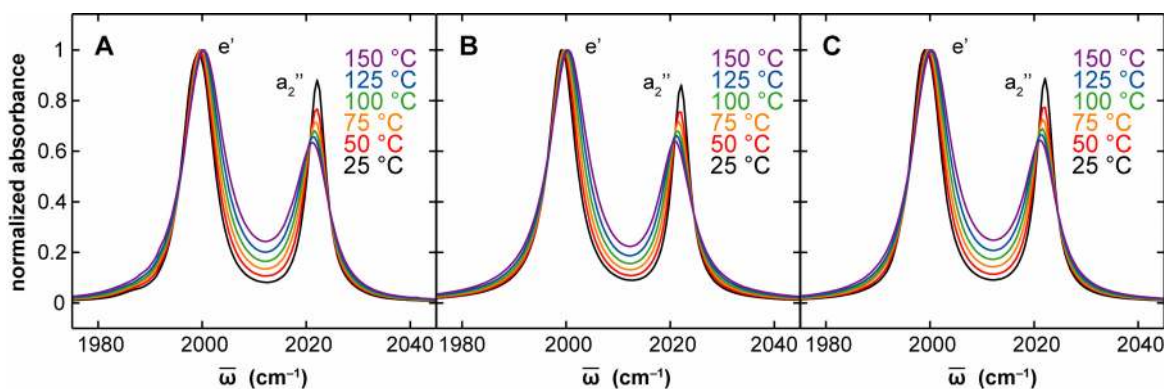

Fig. S1. Temperature dependent FTIR spectra of $Fe(CO)_5$ in *n*-dodecane (**A**), the best fits of the data to two Lorentzian functions (**B**), and the best fits of the data including the effects of coalescence due to exchange of the carbonyl groups by a pseudo-rotation mechanism (**C**). All spectra are normalized to the peak of the e' vibrational mode.

is typical for absorption bands beginning to show coalescence but may also be due to an increase in the homogeneous line width resulting from an increase in the rate of vibrational dephasing with temperature.

In order to quantitatively understand the changes in line shape, the FTIR spectra at each temperature were fit to two Lorentzian functions, with the best fit curves shown in Fig. S1B. The FTIR spectra were also simulated in the presence of fast exchange following the method outlined by Grevels, McClung, and co-workers for purely homogeneous broadening (*S13*). DFT calculations were used to supply the fixed parameters necessary for the simulation procedure. The best fit simulations were achieved using an iterative procedure (refer to section ID) in which all variables (center frequencies, dephasing rates, intensities, and exchange rate) were adjustable, and these curves are shown in Fig. 1C. The iterative routine typically produced exchange rate constants on the order of $0.1 \ ps^{-1}$, but we do not cite exact numbers or errors due to the potentially large systematic error in this procedure.

Comparing the Lorentzian fits (Fig. S1B) with the exchange simulations (Fig. S1C), both models appear to adequately reproduce the experimental data. It is useful to note that the Lorentzian fits are equivalent to an exchange simulation with an exchange rate constant of zero. The similarity of the two simulations highlights the difficulty in using linear IR spectroscopy alone to understand the exchange dynamics underlying these lineshapes. The changes with temperature are subtle, and without data over a broad range of temperatures sufficient to show complete coalescence of the two bands into one, it is not possible to extract accurate information on the exchange dynamics.

Despite the limitations of linear IR spectrosocpy, 2D-IR spectroscopy, even at one single temperature, provides direct information on the exchange dynamics and gives conclusive evidence that exchange is a real and importance process on the IR time-scale. The 2D-IR data indicate that exchange occurs on a time-scale less than 10 ps, which is sufficiently rapid to contribute to the changes in FTIR lineshape in Fig. S1A. Thus, the most physically reasonable method to quantitatively understand the line shapes are through models which include effects of exchange (Fig. S1B). These results also imply that the analysis given by Grevels et al. for the line shapes of $Fe(CO)_3(\eta^4$-1,5-cyclooctadiene) is physically sound and could be further confirmed with 2D-IR spectroscopy.

III.   Effects of vibrational relaxation

In this work we analyze changes in the 2D-IR spectra of $Fe(CO)_5$ in terms of fluxionality, however, vibrational relaxation processes may also give rise to dynamics in 2D-IR spectra and these possibilities are addressed below. For clarity, we separately address two different processes: population relaxation of quanta in the CO stretch vibrational modes and population transfer between the CO stretch vibrational modes.

A.   Population Relaxation

The CO stretches of organometallic complexes typically relax on a time-scale of many tens of picoseconds to hundreds of picoseconds (*S15-18*). For $Fe(CO)_5$, the e' and a_2'' modes relax on a time-scale of ca. 150 ps by transferring energy into the lower frequency modes of the molecule and ultimately into the solvent, which is a standard paradigm for vibrational relaxation in the condensed phase (*S19, S20*). Fig. S2A shows kinetic data for the e' vibrational mode from broadband IR-pump, IR-probe experiments on $Fe(CO)_5$ in *n*-hexane. The data are well fit to a single exponential decay with a time constant of 154 ± 7 ps. The a_2'' vibrational mode decays on a similar time-scale of 156 ± 10 ps. It is not surprising that the two vibrational modes exhibit nearly identical population relaxation times because these modes efficiently exchange energy on a much faster time-scale than population relaxation.
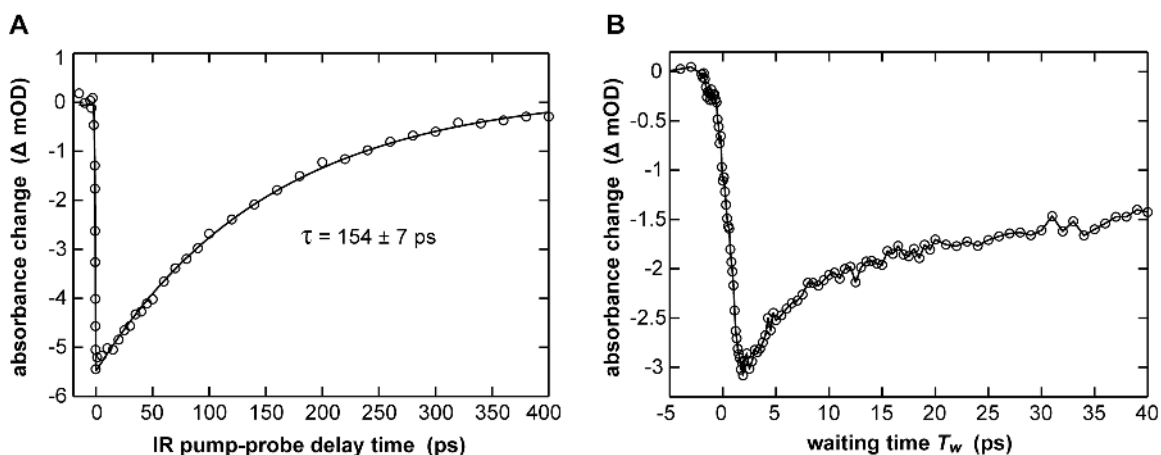

Fig. S2. (**A**) Vibrational population relaxation kinetics of the e' CO vibrational mode at 2000 cm^{-1} from broadband IR pump-probe data of $Fe(CO)_5$ in *n*-hexane. Solid line represents a single exponential fit to the data with a time constant of 154 ± 7 ps. (**B**) Kinetics of the negative diagonal peak for the e' vibrational mode of $Fe(CO)_5$ in *n*-dodecane from 2D-IR data at room temperature (18 ˚C).

This relaxation process causes a decay in the amplitude of the 2D-IR spectra with increased T_w. The 2D-IR spectra in Fig. 2 are normalized with respect to the maximum absorption at each T_w (the e' diagonal absorption) and this normalization eliminates the decay in amplitude from population relaxation. The kinetics of the e' diagonal absorption used for normalization are shown in Fig. S2B in order to provide a quantitative measure of the decay in the signal amplitude. The magnitude of the absorption rises on a time-scale limited by the laser pulse and then initially decays due to energy transfer out of this mode as a result of fluxionality. The longer decay is the same decay observed in Fig. S2A and results from population relaxation of the CO stretches into lower frequency vibrations. Note that on the time-scale of fluxionality (8 ps), approximately 5% of the vibrational energy initially imparted in the CO stretch vibrations has undergone population relaxation to the lower frequency vibrational modes.

In order to understand the 2D-IR data in terms of fluxionality, we analyze the ratio of the off-diagonal to diagonal intensity for the negative signals the a_2'' and e' vibrational modes as a function of waiting time. If population relaxation of these two modes occurred on a time-scale competitive with the energy transfer process and if the rates of vibrational relaxation were different for the two modes, then this ratio would not necessarily eliminate effects from population relaxation. Fortunately, neither of these two cases is true for $Fe(CO)_5$, and the ratio is thus a convenient measure of the energy transfer process and can be modeled without needing to include the effects of population relaxation.

Because population relaxation of the CO stretching modes populates lower frequency modes in the molecule, this process can cause additional changes in the cross peaks of the CO stretches if the lower frequency modes are strongly coupled to the CO vibrations. Rubitsov and coworkers recently reported this effect in a small organic molecule and stressed its potential importance for enhancing cross peak intensities at long T_w (*S21*). We do not observe this effect in $Fe(CO)_5$ for two reasons. First, the CO stretches in $Fe(CO)_5$ relax on a relatively long 150-ps time-scale (Fig. S2A) while the lower frequency modes for organometallic complexes have been shown to relax by transferring energy to the solvent on a shorter time-scale of ca. 50 ps or less (*S16, S22*). The fast relaxation of the low frequency modes in comparison to the high frequency CO stretches prevents vibrational energy from building up in them; thus, the modes do not have sufficient population to strongly contribute to the 2D-IR spectra. Second, as discussed by Rubitsov,

this effect can be observed in 2D-IR spectra as a shift in the cross peak positions. Cross peaks resulting from the anharmonicity between vibrational modes appear in pairs, with one positive and one negative peak. The separation between these two peaks is determined by the magnitude of the anharmonic coupling between the vibrational modes and the line width of the absorptions. In the case discussed by Rubitsov, vibrational relaxation populates new vibrational modes with smaller magnitude anharmonic coupling and this difference manifests itself as a decrease in the separation between the negative and positive peak pair. In contrast, we do not observe any change in this separation in the 2D-IR spectra of $Fe(CO)_5$. Fig S3 shows 2D-IR spectra at seven different waiting times, and the separation between the positive and negative signals of the two cross peaks is preserved at all T_w, a strong indication that lower frequency modes are not contributing to the spectra. This observation is especially apparent through a comparison of panels E and G of Fig. S3, which depict spectra collected at T_w separated by 25 ps but which appear appear nearly identical. In addition, the negative and positive signals of the two cross peaks appear at exactly the same horizontal
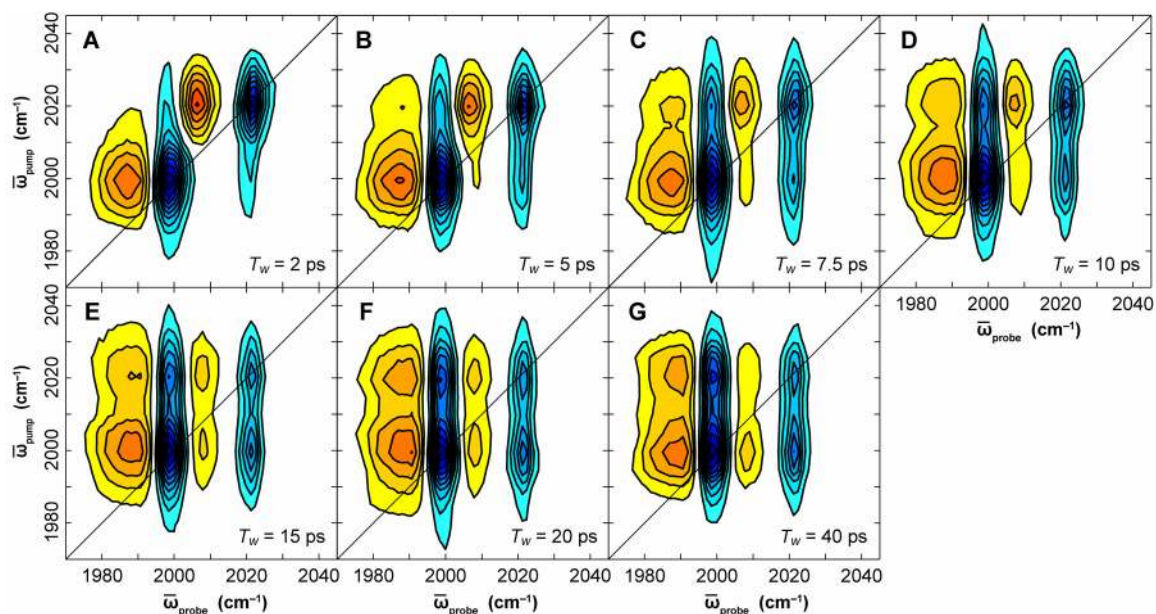

Fig. S3. 2D-IR spectra of $Fe(CO)_5$ acquired at waiting times of T_w = 2 ps (**A**), 5 ps (**B**), 7.5 ps (**C**), 10 ps (**D**), 15 ps (**E**), 20 ps (**F**), and 40 ps (**C**). The data are normalized to the maximum absorption at each T_w, which corresponds to the negative absorption (blue) of the e' vibrational mode (see Fig. S2B for the absolute magnitude of this absorption), and contour lines represent a 10% change in absorption intensity. The spectra shown in Fig. 2 are reproduced here for easy comparison.

positions (probe frequency) as the diagonal peaks vertically displaced from them. This observation is a firm indication that the separation of the negative and positive signals of each cross peak result from the diagonal anharmonicity of the vibrational modes (just like the vertically displaced diagonal peaks) rather than off-diagonal anharmonic coupling between different vibrational modes. Thus, it seems clear that the cross peaks result solely from vibrational energy transfer between the CO stretching vibrations of $Fe(CO)_5$ and vibrational relaxation into lower frequency modes is not important for understanding the dynamics observed in the spectra.

B.   Population transfer

There are only a handful of examples of fast vibrational energy transfer between the carbonyl vibrations of organometallic complexes in the literature (*S17, S18, S23-27*). A rigorously documented example is $Rh(CO)_2(acac)$ (RDC; acac = $C_5H_7O_2$) which has been studied with ultrafast spectroscopy by several groups (*S17, S25-27*). Tokmakoff and coworkers analyzed the 2D-IR spectra of RDC and thoroughly analyzed both coherence transfer and population transfer between the symmetric and asymmetric stretches of the two carbonyls (*S27*). Note that this 2D-IR study used a fully coherent three-pulse Fourier transform technique in which the transfer of a coherence between vibrational modes during the two coherence times affects the 2D-IR spectra. In contrast, the pump-probe 2D-IR spectroscopy used here on $Fe(CO)_5$ does not show the effects of coherence transfer because the bandwidth of IR pump pulse is sufficiently narrow that a vibrational population cannot be created following a coherence transfer event; thus, the coherence transfer does not affect the third-order polarization signal acquired by frequency-resolved homodyne detection of the IR probe pulse. This pump-probe technique is, however, sensitive to population transfer in exactly the same manner as the fully coherent three-pulse Fourier transform 2D-IR spectroscopy.

Tokmakoff and coworkers observed population transfer between the symmetric and asymmetric stretch of RDC on a time-scale of 3 ps, an effect which had also been observed earlier with IR-pump, IR-probe measurements (*S17*). It is difficult to determine whether fluxionality might be relevant to this system without further investigation, but we assume the energy transfer is purely a result of IVR. The question arises if this time-scale of a few picoseconds is general to organometallic complexes such as $Fe(CO)_5$ or if

RDC is a case of unusually efficient IVR. The anharmonicity between the symmetric and asymmetric stretches of RDC was experimentally measured to be 26 cm^{-1} (*S26*) whereas the calculated anharmoncity for the e' and a$_2$'' modes of Fe(CO)$_5$ is a drastically smaller 0.6 cm^{-1}. Note that the anharmonicity of RDC has also been calculated from DFT giving a value of 20.3 cm^{-1} (*S28*), which is in good agreement with experiment. Because the third-order and higher anharmonic terms in the nuclear potential energy are responsible for IVR processes, the small magnitude of the coupling between the modes in Fe(CO)$_5$ suggests that energy transfer should be significantly slower in comparison to RDC (*S20*).

There are two key differences between RDC and Fe(CO)$_5$ which provide simple and intuitive reasons for the differences in the anharmonicities of the CO vibrations for these molecules. First, the symmetric and asymmetric stretches of RDC are exactly localized on the same two CO ligands whereas the e' and a$_2$'' modes of Fe(CO)$_5$ are each localized on different sets of CO ligands. Using the squares of the coefficients of the local mode projection of these vibrations as described in eq. 1, the DFT calculations indicate that the e' and a$_2$'' modes are each greater than 99.9% localized on the equatorial and axial CO ligands, respectively. The difference in spatial overlap of the vibrational modes helps to explain why the anharmonicity for the IR active CO stretches in these two systems is different by more than an order of magnitude. Second, the metal and ligand bonding in RDC and Fe(CO)$_5$ provide some additional insight additional into the differences of these systems. In RDC, the σ-bonding of the two equivalent carbonyls to the metal occurs through the same set of metal orbitals of *d*, *s*, and *p* character. In Fe(CO)$_5$ on the other hand, the σ-bonding of the axial and equatorial carbonyl groups occurs through different metal *d*-orbitals, primarily d$_{z^2}$ for the axial CO groups and d$_{x^2-y^2}$ / d$_{xy}$ for the equatorial CO groups (*S29*). The axial and equatorial CO groups both participate in π back-bonding with the same metal d$_{xz}$ / d$_{yz}$ orbitals, which provides a weaker mechanism for coupling than would be provided by direct σ-bonding with the same set of metal orbitals as is the case in RDC.

Despite the differences in the bonding and vibrational modes of RDC and Fe(CO)$_5$, we are still left to consider a system-bath interaction in which the bath serves to couple the two modes and also accepts the energy difference, or mismatch, between the CO stretch modes. For RDC, Tokmakoff and coworkers propose that the acac ring in the molecule serves as the "bath" to couple the two vibrational modes, and

there is clearly no equivalent for $Fe(CO)_5$. The lowest calculated vibrational frequency in $Fe(CO)_5$ is 53 cm^{-1}, well above the energy mismatch (22.8 cm^{-1}) between the e' and a$_2$'' modes. Instead, the solvent, *n*-dodecane, must serve as the bath in this system. Recent studies have suggested that solvent-assisted IVR, another term which could be used for population transfer with participation of the solvent, is an extremely physically localized process. Pate and coworkers analyzed the IVR dynamics of the acetylenic C–H stretch of a series of progressively larger terminal acetylenes and, as one conclusion, determined that solvent-induced energy relaxation only occurs in close physical proximity to the excited vibrational state (*S30*). These results suggest that solvent-assisted IVR is less likely to occur in $Fe(CO)_5$ because the e' and a$_2$'' vibrational modes are localized on different sets of CO groups. While this consideration does not preclude the energy transfer mechanism, it does indicate the process would be slower than if the vibrations were delocalized over the same set of CO groups.

The considerations outlined in the preceding paragraphs do not definitively prove that solvent-assisted IVR is not occuring in $Fe(CO)_5$. Rather, these considerations are only meant to provide a qualitative argument that IVR in this system is likely to occur on a longer time-scale than has been observed previously in RDC and on a longer time-scale than fluxionality. We have found that we can fully simulate and understand the 2D-IR data without including IVR. In addition, we have examined the temperature dependence of vibrational energy exchange and found that it is in better agreement with fluxionality than IVR, as detailed in section V.

IV.   Simulations

A.   2D-IR spectra

The 2D-IR spectra in Fig. 2 were simulated assuming purely Lorentzian line shapes as given by Lorentzian fits to the room-temperature FTIR spectrum shown in Fig. 1A. This FTIR spectrum is well fit to two Lorentzian functions centered at 1999 and 2022 cm^{-1} with FWHM of 6.3 cm^{-1} and 4.0 cm^{-1}, respectively, indicating that the a$_2$'' and e' peaks are primarily homogeneously broadened. As a result, the 2D-IR spectra should not exhibit any changes attributable to spectral diffusion since these effects result from the sampling of frequencies within an inhomogeneously broadened distribution of frequencies. For off-diagonal contributions to the spectra, harmonic scaling of the intensities and line widths was assumed.

Anharmonic parameters were included in the simulations as calculated by DFT anharmonic frequency calculations (*S31, S32*) for the anharmonicities of each individual mode ($\chi_{a2"} = -6.0 \text{ cm}^{-1}$; $\chi_{e'} = -6.0 \text{ cm}^{-1}$) and between the different modes ($\chi = 0.6 \text{ cm}^{-1}$) and between the two degenerate e' modes ($\chi = -7.9 \text{ cm}^{-1}$). All peaks resulting from vibrational anharmonicity were included in the simulations appropriately scaled relative to the diagonal peaks to account for their relative contribution to the third-order polarization signal.

Vibrational energy exchange was also included in the simulation of the 2D-IR spectra, causing changes in relative intensities of the diagonal and off-diagonal peaks as a function of the waiting time T_w. The kinetics of the vibrational energy exchange were simulated using eq. 4 and standard finite difference methods (*S33*), and the kinetic simulation included convolution with the experimental time resolution of 1 ps. Based on the energy transfer predicted by this kinetic model, the relative intensities of the diagonal and off-diagonal peaks were scaled up or down as appropriate and the intensities of all anharmonic peaks were recalculated accordingly. Spectra were generated by calculating the intensity on a two dimensional grid with a spacing of 0.5 cm^{-1} between each point. The data were then convoluted with the experimental spectral resolution along both frequency axes in order to allow direct comparison between the simulation and experimental data.

B.   Kinetics of vibrational energy exchange

The kinetics of the energy exchange process were simulated using eq. 4 and standard finite difference methods (*S33*). The population of each vibrational mode beginning from time zero was updated in time steps of 50 fs assuming vibrational energy transfer into each mode at a rate defined by eq. 4. In order to account for the degeneracy of the e' vibrational modes, the energy between these two modes was equilibrated (i.e. divided equally) between the modes after each time step of the simulation. The result of this kinetic simulation was then convoluted with a single-sided exponential decay of 1 ps in order to accurately reflect the instrument response function and the time resolution of the 2D-IR experiment. This simulation was performed for different mechanisms by changing the values for $P_{n_i \rightarrow n_f}$ in eq. 4 as appropriate for the mechanism under consideration.

In order to determine the fluxionality rate constant k (see eq. 4) which best reproduces the experimental data, an iterative procedure was used to produce the best fit to the data. The simulations of vibrational energy exchange produce two data sets comparable to the experimental data, one in which the vibrational energy is initially in the a_2'' mode and a second in which the vibrational energy is initially in the e' mode. These two data sets asymptotically approach, at long T_w, values of 2 e' : 1 a_2'' regardless of the mechanism (due to multiple crossings), and a plot of these ratios is directly comparable to the experimental data of the off-diagonal to diagonal ratios (refer to Fig. 3A). In order to find the rate constant k which best fits the experimental data for a given mechanism, an iterative fitting procedure was used in which k was varied until the best agreement with the data was achieved. This fitting procedure also includes a small scaling factor and offset for the simulation curves in order to account for the fact that the experimental off-diagonal to diagonal ratio is affected by relative absorption intensities and line widths. The scaling factor and offset for each curve along with one rate constant k (total of five parameters) were iterated to achieve the best fit with the experimental data. The reported time constants are equivalent to k^{-1}.

C.   Twist mechanism

In order to verify that the 2D-IR method employed in this study is sensitive to the mechanism and transition state of the reaction, we have simulated the data for a twist type rearrangement of the CO ligands in $Fe(CO)_5$, as shown in Fig. S4. This particular twist rearrangement involves the motion of three adjacent CO groups, with one axial CO becoming equatorial, one equatorial CO becoming axial, and one equatorial CO shifting positions but remaining equatorial. As in the Berry pseudo-rotation mechanism, the reactant and product are chemically identical, and the mechanism is distinguished only by the transition state of the reaction, which defines the motion between reactant and product and defines which CO groups are exchanged during the process. We were unable to locate a transition state corresponding to this mechanism using DFT calculations; however, we were able to project the vibrations in the reactant directly onto the vibrations in the product as described by eq. 2, where the rearrangement of CO groups explicitly assumes the mechanism and transition state of the reaction. The coefficients for the projection are given in Fig. S4, where the vibrational normal modes are labeled by their corresponding symmetries, analogous to Fig. 4B. The squares of these coefficients, as given by eq. 3, are given as percentages in the far right column of Fig.
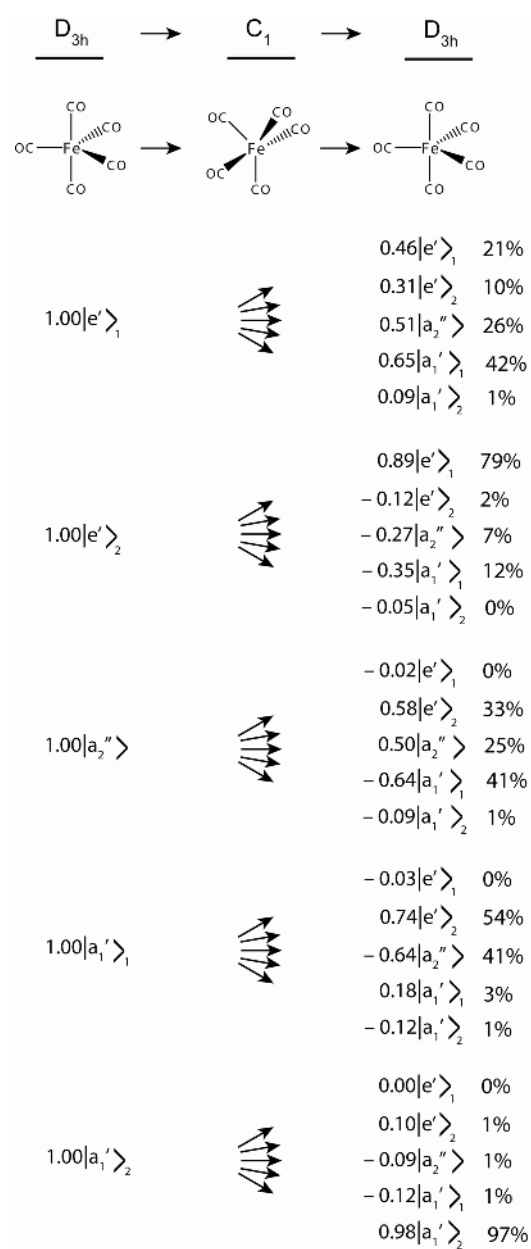
Fig. S4. The splitting of vibrational modes and vibrational energy as predicted for a twist rearrangement of the CO groups in $Fe(CO)_5$

S4 and represent the probability of vibrational energy transferring into the vibrational modes. Since this mechanism proceeds through a transition state of lower symmetry than the Berry pseudo-rotation, the vibrational energy transfer is not limited by symmetry considerations, and it is necessary to explicitly show energy transfer from each mode into all five other vibrational modes. The room-temperature experimental

2D-IR data was fit for this mechanism by the procedure described above (section II B), and the best fit was achieved with a time constant of 3.5 ± 0.4 ps.

In order to provide a rough estimate of the electronic energy barrier for a twist rearrangement of the CO ligands in $Fe(CO)_5$, we constrained the structure to an approximate guess of the transition state geometry and performed a DFT geometry optimization and energy calculation with the constraints. The bond angles (C–Fe–C) between each exchanging CO group and the CO group it replaces were constrained to half the total change in bond angle required to complete the rearrangement. Thus for the three exchanging CO groups, the axial CO which becomes equatorial was constrained to 45°, the equatorial CO which becomes axial was also constrained to 45°, and the equatorial CO which remains equatorial was constrained to 60°. These constraints produced a structure similar to the C_1 structure depicted in Fig. S4. For the DFT calculations, all C–Fe–C bond angles were fixed while all other parameters (bond lengths, Fe–C–O bond angles) were optimized. The calculated energy of the constrained structure is 38.97 kcal/mol higher than the D_{3h} structure of $Fe(CO)_5$.

In order to provide an approximate benchmark of the accuracy of this constrained DFT calculation, we performed a similar calculation for the C_{4v} transtion state of the pseudo-rotation mechanism. For this mechanism, all C–Fe–C bond angles for the exchanging CO groups move by a total of 30° with respect to the one CO group that does not exchange. The exchanging CO groups were thus fixed at 15° from their original position as appropriate. All parameters other than the C–Fe–C bond angles were optimized and the resulting structure was 2.32 kcal/mol higher in energy than the D_{3h} structure of $Fe(CO)_5$. Thus, for the pseudo-rotation mechanism, the calculation with constrained bond angles overestimated the barrier height by only 0.19 kcal/mol in comparison to our previous calculation on the fully optimized transition state structure. Given the accuracy of this method for the pseudo-rotation mechanism, it appears reasonable to assume that the true barrier for the twist rearrangement would be at least one order of magnitude (21 kcal/mol) greater than the calculated barrier for the pseudo-rotation mechanism (2.13 kcal/mol). Unfortunately, our calculations attempting to locate a true stationary point on the electronic potential energy surface of $Fe(CO)_5$ corresponding to the twist rearrangment consistently relaxed to a lower energy stationary point.
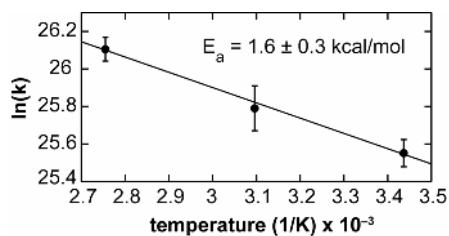
Fig. S5. Arrhenius plot for the rate of fluxionality at 18, 50, and 90 °C as determined by 2D-IR experiments at these temperatures. Line is a linear fit to the data points, giving a slope and corresponding activation energy of 1.6 ± 0.3 kcal/mol.

V.   Arrhenius Plot

2D-IR data were collected at 18 ˚C (room temperature), 50 ˚C, and 90 ˚C, and the off-diagonal to diagonal ratios at all three temperatures were fit using the procedure outlined in section IV B to the pseudo-rotation mechanism, giving time constants of 8.0 ± 0.6 ps, 6.3 ± 0.8 ps, and 4.6 ± 0.4 ps, respectively. An Arrhenius plot of these data is shown in Fig. S5, and gives a straight line with a slope corresponding to an activation energy of 1.6 ± 0.3 kcal/mol.

The temperature dependence of the 2D-IR data is consistent with our interpretation that the vibrational energy exchange between the e' and a_2'' modes results from the physical exchange of carbonyl groups in $Fe(CO)_5$. Nevertheless, solvent-assisted intramolecular vibrational relaxation (IVR) can also cause vibrational energy exchange (see section IIIB) and may also exhibit temperature dependence. IVR is caused by anharmonic coupling between vibrational modes, and the solvent assists this process by receiving or supplying the difference in energy between the modes. The ability of the solvent to mitigate the energy mismatch relies on the presence of liquid phonons (instantaneous normal modes of the solvent) at the frequency of the energy mismatch (22.8 cm^{-1}), and the occupation number of the phonons at this frequency is linearly proportional to the rate of the transition (*S20, S34*). The phonon occupation number, n, is expressed by the well know relation (*S35*) eq. S1,

$$n = \left[\exp\!\left(E_p / k_b T\right) - 1 \right]^{-1},$$ (S1)

where E_p is the phonon energy, k_b is the Boltzmann constant, and T is temperature. Based on this expression, the occupation number for phonons at 22.8 cm^{-1} should increase by 26% between 18 ˚C and 90

˚C, and thus the rate of IVR should also increase by 26%. We instead observe a 74% ± 20% increase in the rate over this temperature range.

IVR may also exhibit a temperature dependence through the other factors which enter into a calculation of the IVR rate, such as the anharmonic matrix elements connecting the vibrational modes and the phonon density of states. It has been suggested that both of these properties tend to reduce the rate of IVR at higher temperatures and in some cases, overcome the contribution of the phonon occupation number. As a result, the rate of vibrational relaxation has been observed to decrease at higher temperatures in some circumstances (*S34*). Given these considerations, it seems reasonable to expect that an increase of 26% based eq. S1 is an upper estimate for the change in the rate of IVR with temperature, and the temperature dependence we observe in the 2D-IR data is not consistent with this estimate.

References

S1.   P. Hamm, R. A. Kaindl, J. Stenger, *Opt. Lett.* **25**, 1798 (2000).

S2.   J. Helbing, personal communication to J. F. Cahoon, Aug. 31, 2006.

S3.   J. Bredenbeck, J. Helbing, P. Hamm, *J. Chem. Phys.* **121**, 5943 (2004).

S4.   J. R. Taylor, *An Introduction to Error Analysis*. (University Science Books, Sausalito, ed. 2, 1982).

S5.   Y. S. Kim, R. M. Hochstrasser, *J. Phys. Chem. B* **110**, 8531 (2006).

S6.   T. Ito, T. Hamaguchi, H. Nagino, T. Yamaguchi, J. Washington, C. P. Kubiak, *Science* **277**, 660 (1997).

S7.   C. H. Londergan, C. P. Kubiak, *Chem. Eur. J.* **9**, 5962 (2003).

S8.   F. W. Grevels, J. Jacke, W. E. Klotzbucher, C. Kruger, K. Seevogel, Y. H. Tsay, *Angew. Chem., Int. Ed. Engl.* **26**, 885 (1987).

S9.   F. W. Grevels, J. Jacke, K. Seevogel, *J. Mol. Struct.* **174**, 107 (1988).

S10.   H. Angermund, F. W. Grevels, R. Moser, R. Benn, C. Kruger, M. J. Romao, *Organometallics* **7**, 1994 (1988).

S11.   J. J. Turner, F. W. Grevels, S. M. Howdle, J. Jacke, M. T. Haward, W. E. Klotzbucher, *J. Am. Chem. Soc.* **113**, 8347 (1991).

S12.   J. J. Turner, C. M. Gordon, S. M. Howdle, *J. Phys. Chem.* **99**, 17532 (1995).

S13.   F. W. Grevels, K. Kerpen, W. E. Klotzbucher, R. E. D. McClung, G. Russell, M. Viotte, K. Schaffner, *J. Am. Chem. Soc.* **120**, 10423 (1998).

S14.   H. L. Strauss, *J. Am. Chem. Soc.* **114**, 905 (1992).

S15.   E. J. Heilweil, R. R. Cavanagh, J. C. Stephenson, *J. Chem. Phys.* **89**, 230 (1988).

S16.   T. P. Dougherty, E. J. Heilweil, *Chem. Phys. Lett.* **227**, 19 (1994).

S17.   J. D. Beckerle, M. P. Casassa, R. R. Cavanagh, E. J. Heilweil, J. C. Stephenson, *Chem. Phys.* **160**, 487 (1992).

S18.   S. M. Arrivo, T. P. Dougherty, W. T. Grubbs, E. J. Heilweil, *Chem. Phys. Lett.* **235**, 247 (1995).

S19.   Y. Q. Deng, R. M. Stratt, *J. Chem. Phys.* **117**, 1735 (2002).

S20.   H. J. Bakker, *J. Chem. Phys.* **98**, 8496 (1993).

S21.   D. V. Kurochkin, S. R. G. Naraharisetty, I. V. Rubtsov, *Proc. Natl. Acad. Sci. U.S.A.* **104**, 14209 (2007).

S22.   T. Q. Lian, S. E. Bromberg, M. C. Asplund, H. Yang, C. B. Harris, *J. Phys. Chem.* **100**, 11994 (1996).

S23.   A. Tokmakoff, B. Sauter, A. S. Kwok, M. D. Fayer, *Chem. Phys. Lett.* **221**, 412 (1994).

S24.   M. Banno, S. Sato, K. Iwata, H. Hamaguchi, *Chem. Phys. Lett.* **412**, 464 (2005).

S25.   D. E. Thompson, K. A. Merchant, M. D. Fayer, *J. Chem. Phys.* **115**, 317 (2001).

S26.   M. Khalil, N. Demirdoven, A. Tokmakoff, *J. Phys. Chem. A* **107**, 5258 (2003).

S27.   M. Khalil, N. Demirdoven, A. Tokmakoff, *J. Chem. Phys.* **121**, 362 (2004).

S28.   A. M. Moran, J. Dreyer, S. Mukamel, *J. Chem. Phys.* **118**, 1347 (2003).

S29.   T. A. Albright, J. K. Burdett, M.-H. Whangbo, *Orbital Interactions in Chemistry*. (John Wiley & Sons, Inc., New York, 1985).

S30.   H. S. Yoo, M. J. DeWitt, B. H. Pate, *J. Phys. Chem. A* **108**, 1348 (2004).

S31.   DFT calculations were performed at the BP86 level using the basis sets 6-31+g(d) for C and O and LANL2DZ for Fe with the program Gaussian 03, Revision C.02, M. J. Frisch, *et. al.*, Gaussian, Inc., Wallingford CT, 2004.

S32.   V. Barone, *J. Chem. Phys.* **122**, 014108 (2005).

S33.   J. I. Steinfeld, J. S. Francisco, W. L. Hase, *Chemical Kinetics and Dynamics*. (Prentice-Hall, Inc., Upper Saddle River, ed. 2, 1989).

S34.   A. Tokmakoff, B. Sauter, M. D. Fayer, *J. Chem. Phys.* **100**, 9035 (1994).

S35.   D. Chandler, *Introduction to Modern Statistical Mechanics*. (Oxford University Press, Inc., New York, 1987).